



Porous structure and fluid partitioning in polyethylene cores from 3D X-ray microtomographic imaging

M. Prodanović^a, W.B. Lindquist^{a,*}, R.S. Seright^b

^a Department of Applied Mathematics and Statistics, Stony Brook University, Stony Brook, NY 11794-3600, USA

^b New Mexico Petroleum Recovery Research Center, New Mexico Institute of Mining and Technology, 801 Leroy Place, Socorro, NM 87801, USA

Received 7 July 2005; accepted 24 November 2005

Available online 20 December 2005

Abstract

Using oil-wet polyethylene core models, we present the development of robust throat finding techniques for the extraction, from X-ray microtomographic images, of a pore network description of porous media having porosity up to 50%. Measurements of volume, surface area, shape factor, and principal diameters are extracted for pores and area, shape factor and principal diameters for throats. We also present results on the partitioning of wetting and non-wetting phases in the pore space at fixed volume increments of the injected fluid during a complete cycle of drainage and imbibition. We compare these results with fixed fractional flow injection, where wetting and non-wetting phase are simultaneously injected at fixed volume ratio. Finally we demonstrate the ability to differentiate three fluid phases (oil, water, air) in the pore space.

© 2005 Elsevier Inc. All rights reserved.

Keywords: Porous media; Pore network models; Pore microstructure; Fluid displacement; Drainage; Imbibition

1. Introduction

The development of computational methods to analyze the three-dimensional (3D) microstructure of porous media [1–13] has experienced tremendous invigoration with the advent of synchrotron X-ray computed microtomography (CT) [14], specifically since CT produces huge quantities of 3D data sets, at micron scale resolution in, relatively speaking, short time. It is now fairly common practice to perform fluid transport simulations (e.g. [11,15–22]) in medium realizations based upon 3D CT images. More recently CT technology has been extended to the ability to contrast fluids in the pore space of core samples (air–water in sand packs [23], oil–water in Berea cores [24–26], oil–water in sand packs [27], oil–water in glass bead packs [28], and air–oil in Berea cores [29]), and therefore to the study of fluid partitioning in the 3D pore space. Such studies have

the promise to contribute necessary model verification data for fluid transport simulations as well as fluid parameter input (e.g., interphase surface contact areas) for transport models. As CT imaging times are much longer than flow time scales, CT imaging of fluids must be done at a fixed fluid state. Such studies have been done at residual fluid conditions. In this study, we report on fluid partitioning during a complete drainage and imbibition cycle during which CT images were taken after fixed volumes of displacing fluid were incrementally injected. We also report on a second study in which images were obtained after large volumes of both non-wetting and wetting phase were simultaneously injected at fixed volume ratio (fixed fractional flow conditions).

These studies were performed in strongly oil-wet, polyethylene cores. The average pore size in the cores is representative of sandstone standards such as Berea and Fontainebleau; however the polyethylene grain is very homogeneous, which is most desirable for CT studies. In addition, the polyethylene surface is much smoother than is the grain surface in sandstones, simplifying issues relative to surface wetting. On the negative side, the 40–50% porosity of such cores is at least twice that of

* Corresponding author. Fax: +1 631 632 8490.

E-mail addresses: masha@ams.sunysb.edu (M. Prodanović), lindquis@ams.sunysb.edu (W.B. Lindquist), randy@prrc.nmt.edu (R.S. Seright).

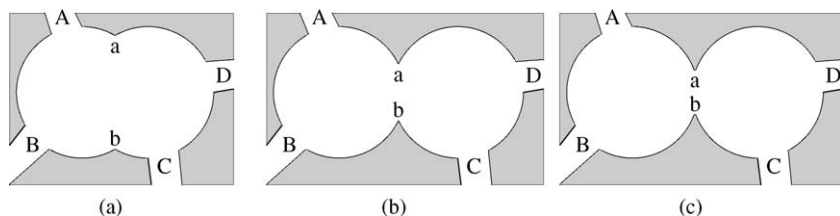


Fig. 1. An illustration of the intuitive difficulty in determining single pore bodies. In each subfigure, void space (white) is accessed through four channels entering at A, B, C and D.

sandstone standards, but is comparable to unconsolidated media.

The larger porosity of these polyethylene cores forces the exploration of a second issue in addition to addressing fluid partitioning. It is standard thinking, and indeed standard practice in network flow modeling, to regard the void structure in geological porous media as a network of pore bodies (“pores” for short) connected to each other via channels. A number of numerical algorithms have been developed [1,3–10,12,13] to analyze CT images and extract pore–channel (or pore–throat) networks.

Central to all algorithms is the labeling of each pore voxel with a value which measures the distance to the closest grain voxel. The pore medial axis (or skeleton) is a minimal deformation retract of the void space which preserves topological properties of the pore space and is centrally located along the pore space. The medial axis (MA) can be organized into paths and branch clusters, utilizing either 26-adjacency or λ -adjacency [8]. The backbone of the MA has all (non-existing) dead-end paths pruned.

Early attempts used property measurements from the MA backbone to characterize the pore space in reconstructed rock [1] and CT images of real rock [4]. Existing algorithms to extract pore networks can be classified into two types, pore-body detecting [5,9,10,13] and throat constructing [3,6,8,12]. Algorithms of the former type locate pore bodies first and throats secondarily. With one exception, all existing methods construct pores around voxels having local maximum in the distance measure (and throats around voxels having local minimum in the distance measure). The algorithms differ on the details by which neighboring void voxels are uniquely associated to a particular maximum and how neighborhoods may be further merged, resulting in a final set of pores. The exception [9] is based upon Delaunay tessellation. The method has only been demonstrated for regular sphere packings; extension of the method to real porous media is difficult. Throat constructing algorithms consist of two steps, locating the throat position and constructing the throat surface. The constructed throat surface is either planar or non-planar. As the orientation of a planar throat is defined by a single (normal) direction, planar throat surface finding is done either by testing in a fixed, finite number of directions (the multi-orientation scanning method of Zhao et al. [3] and earlier similar works [30–32]) or by determining the normal from the MA [8]. Planar throats are located at positions where (an approximation to) the hydraulic radius is locally minimum. Throat constructions in [7] and [12] are based upon the location and construction of minimal area throats; the throat surface is not restricted to be planar.

Cores of 40–50% porosity present a particular challenge to pore partitioning algorithms. The specific issue is the problem of extracting a pore–throat network that is both geometrically consistent and intuitively correct. As there is a strong complementarity between finding throats or finding pore bodies as the principal algorithmic implementation, this issue is germane to either approach.

We argue that throat assignments should be geometrically consistent; specifically each throat should separate exactly two pore bodies and throats should not cross each other (though touching is possible). In the network algorithms currently in use, there appears to be no guarantee in any algorithm that throat geometries (either when found explicitly or implicitly) will enforce the two-body separation requirement without crossing. (As an example, though the pore-body finding algorithm based upon inscribed spheres [10] guarantees pairwise touching of pores, it is *assumed* that if one pore connects to n other pores, it does so through n separate throats. Inscribed sphere fitting ignores some fraction of the void space. In this ignored region, no checking is performed to determine whether the geometric positioning and orientation of the n throats implies they are indeed separate and do not cross.) Pore-network finding algorithms have typically been verified on sphere packings (ranging from hexagonally close packed to cubic packed) which repeat a unit cell that consists of non-crossing throats. In general these algorithms then work well on low porosity porous media which are roughly “comparable in geometrical complexity” to such packings. However, we find that the complexity in real media produces unexpected geometries.

By intuitively correct networks, we refer to the question of determining whether a region of void space is to be considered a single pore or more than one pore. Fig. 1 uses a 2D example to illustrate that such judgments are use-specific. The figure illustrates three example void spaces. The question of whether the void space in each case is to be considered a single pore or two bodies, i.e. whether the cross section a–b is considered as a throat, is subjective. From a geometric perspective, in which a throat is considered to be a cross section of local minimum hydraulic radius (the ratio of cross-sectional area:perimeter) [41], all three examples would be considered as showing two pores. In all three illustrations, the cross section a–b has been sketched to have larger hydraulic radius than any of the four channel openings. Therefore from the perspective of primary drainage (the void space is occupied by wetting fluid and is to be displaced by non-wetting fluid via one of the connecting channels), the entire void space will be invaded by non-wetting fluid, implying that the void space is acting as a single pore.

The two conflicting viewpoints of the void space would yield very different pore parameter characterization (e.g., volume, connectivity). We believe a majority would agree that an intuitive perspective would state that (a) represents a single pore while (c) represents two pores.

Our point therefore is that algorithms for extraction of pore networks, whether based on throat- or pore-detecting algorithms, each of which operate on a well defined principle, must be modified by an “intuitive” decision making criterion to resolve issues of the type related to Fig. 1 and by geometrical checking for crossing throats and other inconsistencies in the resulting pore network. The “intuitive” decision is implemented in the pore-body detecting algorithms via a merging algorithm (whose details vary slightly from algorithm to algorithm) to decide which voxels lie in the neighborhood of (i.e., belong to the same pore associated with) each local maximum-distance voxel. Beyond the implementation of this intuitive decision, no further checking of the geometrical consistency of the pore network is performed by these pore–body detecting methods.

The two throat detection algorithms used in this paper define a throat as a local minimum in the cross sectional area of the void space, where local cross section is well defined relative the void space MA [33,34]. Before throats are detected, an additional criterion is implemented to prevent throat searches interior to a void space that appears to have the characteristics of a single pore. This is the implementation of the “intuitive” decision and is based upon a merging criterion for branch clusters (and paths connecting them) on the MA backbone [6]. In void locations where the criterion does allow for a throat search, a rigorous attempt is made to find throat locations. Throat finding is then followed by a pore-network organizing algorithm that checks network consistency by rejecting throat intersections and other topological irregularities that break the “one throat separates exactly two pores” requirement.

In Section 2 we discuss these network consistency algorithms as well as those implemented for analysis of the fluid partitioning in the void space. Our geometrical analysis of X-ray computed microtomographic rock images is based upon improvements and extensions to the 3DMA-Rock software package [35,36]. The primary 3DMA-Rock algorithms utilized in this analysis of porous medium microstructure are void/solid segmentation, void space MA generation and modification, throat finding, organization of the pore space into a network of pores connected by throats, and characterization of the pores and throats in the network. Fluid partitioning analysis can be done independently of the pore–throat network or can be correlated with the geometry of the pore–throat network. The algorithms utilized to analyze fluid partitioning include fluid segmentation, fluid interface surface reconstruction, individual fluid blob identification, and statistical description of the fluid partitioning in terms of either individual blobs or pores. In Section 3 we present the results for both pore–throat network analysis of the polyethylene cores as well as an analysis of fluid partitioning under drainage, imbibition and fixed fractional flow.

2. Materials and methods

2.1. CT imaging

Two polyethylene cores were cut and milled from commercially manufactured rods (Small Parts, Inc.). Relevant bulk characterization of each core and the region analyzed are presented in Table 1. All flow/imaging experiments were performed at ambient temperatures. Two fluid phases were utilized, a water phase (water containing 1% NaCl and 0.1% CaCl₂) and an oil phase (hexadecane doped with 15%, by weight, bromohexadecane). The two cores were initially saturated (injection into dry core) with the oil phase. Vacuum was applied to the outlet end of each core to ensure full saturation of the dry cores.

Core P_O was imaged at saturated oil conditions. It was then subjected to a drainage sequence consisting of incremental, fixed pore volume (pv) injections of the water phase according to the schedule in Table 2, row 1. (The first injection was of 0.54 pv water, followed by another 0.54 pv, for a total of 1.08 pv, etc.) Once 64.5 pv of water was injected, an imbibition sequence of oil injections followed as listed in row 2 of the table. The core was scanned after each injection state. After each image was taken, the core was rotated back to the same initial position to allow for the direct comparison of a common imaged region throughout the entire flooding sequence.

The images on P_O were taken at a voxel size of 4.10 μm using the ExxonMobil beam line X2B at the National Synchrotron Light Source, Brookhaven National Laboratory. The 29.0 mm³ volume imaged consisted of a section across the core diameter half way along the length of the core. Use of a workstation with 1 GByte of RAM allowed analysis of only 7.12 mm³ (450 × 450 × 510 voxels) of the imaged region.

Although fluid injection was controlled using high precision, high pressure syringe pumps (Teledyne ISCO), it is difficult to inject fluid in amounts smaller than 0.5 pv. (Given the total core

Table 1
Physical characterization of the two polyethylene samples

Sample	Diameter (mm)	Length (mm)	Bulk porosity (%)	Core volume (mm ³)	Imaged volume (mm ³)	Analyzed volume (mm ³)
P_O	6.5	35	~40	1161	29.0	7.12
P_M	6.5	53	~40	1759	28.8	17.71

Table 2
Flow sequences performed in the two polyethylene samples

Fluid injected	Cumulative amount (pv)						
	P_O						
Water	0.54	1.08	1.61	2.69	5.4	10.7	64.5
Oil	0.54	1.08	1.61	2.69	5.4	10.7	64.5
	P_M						
Oil:water ratio	100:0 ^a	90:10	80:20	50:50	0:100	100:0 ^b	
Total fluid (pv)	28.41 ^a	8.28	9.46	9.46	10.65	9.46 ^b	

^a Injection into dry core.

^b Injection following 0:100 flood.

volume and its porosity, 0.5 pv is equivalent to 0.25 ml fluid.) To achieve greater control over fluid ratios, sample P_M was flooded with much larger pv's at fixed fractional flow (i.e., simultaneous injection of oil and water phase at fixed volumetric ratio). The sequence of injections is also given in Table 2. (For example, the second injection in the sequence input 8.28 pv's of fluid consisting of oil and water phase in volumetric ratio 90:10.) Though the fluids, at appropriate volume ratio, were injected simultaneously into the end cap at the inlet of the core (which was oriented vertically), we rely on capillary forces and the void space geometry in the core to produce mixing of the fluids. Again a region of 28.8 mm^3 centrally located down the core was imaged, now at a voxel size of $4.091 \mu\text{m}$. Use of a workstation with 2 GByte RAM allowed for analysis of 17.71 mm^3 ($715 \times 715 \times 506$ voxels) of the imaged region.

Note that three injection experiments (at 95:5, 20:80 and 10:90 oil:water volume ratios), performed at the appropriate times during the experimental sequence on P_M , failed for technical reasons (e.g., X-ray beam failure) and are not included in the analysis.

2.2. Segmentation

Analysis requires distinguishing the X-ray attenuation coefficient signals of water, oil and polyethylene phases in the images on a voxel-by-voxel basis. The addition of bromohexadecane to the hexadecane improves the X-ray attenuation contrast between the oil phase and water/polyethylene, however contrast between water and polyethylene is problematic. The location of the solid phase in each core is therefore determined from the oil saturated image; solid location in subsequent images in the flooding sequence is inferred from its location in the oil saturated image. We utilize a segmentation algorithm based on indicator kriging [37] to determine the interface between solid and oil phase in the oil saturated image; the segmentation algorithm is also applied to the pore space to determine the oil–water interface in subsequent images. Thus, at each application, indicator kriging is only segmenting two phases. The indicator kriging algorithm is initialized with two attenuation coefficient thresholds T_0 and T_1 . Any voxel with coefficient below T_0 is assumed to belong to the lower attenuating phase, and any voxel with coefficient higher than T_1 is set to the higher attenuating phase. The classification of voxels with coefficient values between T_0 and T_1 is based on maximum likelihood estimation utilizing a two point covariance function developed from the unsegmented image. This approach results in a smooth interface between the two phases.

2.3. Image registration

Let I_{oil} denote the first (oil saturated) image in an injection sequence, and I_j denote a later image in the sequence. While the rotation and translation stages of the CT scanner return the core to its original position (relative to the beam) with great precision, we have found that small translational shifts can occur between the images. We believe these movements are pressure transient induced when the fluid injection pumps are cycled

on/off for the post injection period when the core is imaged. We correct for small translational shifts, (dx, dy, dz) , of I_j relative to I_{oil} as follows:

- (1) Consider subregions R_{oil} and R_j , each of size N^3 voxels, centered on the same (i, j, k) voxel location in each of the images I_{oil} and I_j , respectively.
- (2) Identify the oil phase in each subvolume (i.e., perform an oil/“other phase” segmentation, where “other phase” is undifferentiated solid/water).
- (3) For each shift (dx, dy, dz) of R_j relative to R_{oil} , compute the number $n_o(dx, dy, dz)$ of oil segmented voxel locations that overlap in the two subregions. Define $f_o(dx, dy, dz) = n_o(dx, dy, dz)/(p_o N^3)$, where p_o is the oil phase fraction in R_{oil} .
- (4) Let (dx, dy, dz) denote the shift that maximizes f_o .

While this procedure could be applied to the entire images I_{oil} and I_j , this would be very CPU intensive. We therefore repeat the above procedure (steps 1–3) on a number of subregions from various locations in the images (determining N and the number of subregions is somewhat ad hoc). For each translation (dx, dy, dz) , let $\bar{f}_o(dx, dy, dz)$ be the average of the fractions f_o obtained from all the analyzed subregions. The translation (dx, dy, dz) that maximizes \bar{f}_o is the one to be used to align the images.

Given the rotational nature of CT imaging, it would appear that core shifts might consist of a combination of a translation along the core cylinder (z -direction) and a rotation in the x – y plane. Using a rotation registration algorithm analogous to the translation one above, we have explicitly checked for rotation effects and found none. This adds confidence to our statement that the minor shifts observed result solely from translations produced from transients in applying/relaxing pumping pressure in the fluid injection tubes before and after each image.

2.4. Medial axis extraction and modification—pore regions

Extraction of the MA [33,34] of the void phase provides a powerful search tool for throat finding algorithms [8,38,39] as well as for pore characterization algorithms that do not explicitly detect throats [5,40]. A MA consists of a network of digitized curves (which we refer to as paths) and digitized versions of vertices (which we refer to as branch clusters). In a pore–channel description of a porous medium, a channel is topologically a tube and is identified with a unique path in the void space MA. As a pore body connects several channels, from a topological point-of-view a pore body should be identified with a single branch cluster. However, as the MA is defined geometrically using a metric, rather than topologically, a single pore may consist of more than one branch cluster plus additional paths that pairwise connect these branch clusters [6].

As our throat finding algorithms perform a one path—one throat search, we modify the MA using the concept of “close clusters” to define single pore regions on the MA and prevent throat searches on these sections.

For brevity, we refer to branch clusters identified as lying within the same pore body as “close clusters.” Close clusters are defined via the following criterion [6]. Consider a path of N voxels joining two clusters C_1 and C_2 . Let v_{1j} denote a voxel belonging to C_1 . Let b_{1j} denote the L_∞ distance from v_{1j} to the closest solid voxel. Let $B_1 = \min_j\{b_{1j}\}$. Define B_2 analogously. $B_i, i = 1, 2$ is a measure of the distance from C_i to the solid surface. If $N < \max\{B_1, B_2\} + 2$, clusters C_1 and C_2 (and paths that join them) are considered to be close (belong to a single pore). The choice of the L_∞ metric is based upon use of a digitized object. The L_2 metric and a test employing $L < \max\{B_1, B_2\}$ where L is actual L_2 path length could be used instead. The MA is modified by merging each set of close clusters and the paths that join them to form a single branch cluster object.

The identification of dead-end pores involves the same ambiguity as does the question of deciding whether a single void space is two pores or one. Thus the same decision criterion can be applied to determine dead-end pores (as in [10]). As our ultimate interest is in fluid motion, and as dead-end pores do not contribute to the percolating backbone of the void space, we instead ignore each dead-end pore by absorbing it into its neighboring percolating pore. This is achieved by eliminating from consideration (pruning) all dead-end paths on the MA. Note that paths that exit through the boundary of the imaged area are not considered dead ends and are not eliminated.

Remaining paths on the MA (i.e., those not merged with close branch clusters or pruned) provide the set of search paths on which the throat detection algorithms operate.

2.4.1. Path curvature, torsion and tortuosity

The robust throat searching technique discussed in Section 2.6.1 requires identification of local maxima in curvature and torsion on each MA path. The *curvature* κ of a parameterized differentiable curve $\vec{r}(t)$ of arc length ds and unit tangent vector $\vec{T} = \vec{v}/|\vec{v}|$, $\vec{v} = d\vec{r}/dt$, is defined as the magnitude of the derivative $d\vec{T}/ds$ and can be written

$$\kappa = |\vec{v} \times \vec{a}| |\vec{v}|^{-3}, \quad \vec{a} = d\vec{v}/dt. \quad (1)$$

The tangent \vec{T} , the unit normal vector $\vec{N} = (\frac{d\vec{T}}{dt} / |\frac{d\vec{T}}{dt}|)$, and the binormal vector $\vec{B} = \vec{T} \times \vec{N}$ form a right-handed coordinate system (the Frenet frame) at each point of the curve. The *torsion* $\tau = -(\vec{B} \cdot \vec{N})$ is the rate at which the osculating plane defined by \vec{T} and \vec{N} twists about \vec{T} as a function of arc length along the curve. In practice the torsion is computed via

$$\tau = \det \begin{vmatrix} x' & y' & z' \\ x'' & y'' & z'' \\ x''' & y''' & z''' \end{vmatrix} |\vec{v} \times \vec{a}|^{-2}. \quad (2)$$

Finally, the *geometrical path tortuosity* is defined as the ratio of the length of a path to the Euclidean distance between its endpoints [4].

2.5. The throat finding algorithms

With the exception of planar throats in the work of Liang et al. [8], throat surfaces are typically found by minimizing cross-

sectional area rather than hydraulic radius, though all throat algorithms can be trivially converted to minimization based upon either criterion. Each of the throat-finding algorithms employs some degree of approximation. In this work we employ a Dijkstra-based algorithm that has been previously tested on Fontainebleau and Berea sandstones having porosities in the range 7.5–22% [6,7,24–26] and a wedge-based algorithm that has been tested on 70–80% porosity vesiculated basalts where the pores result from bubble nucleation and expansion prior to solidification of magma [12]. As stated, these algorithms are applied to those MA paths that have been determined to neither lie within a pore nor enter a dead-end pore.

The throat finding routine based on Dijkstra's shortest path algorithm is described in [6,38]. Using a 3D grassfire algorithm, a MA path is dilated orthogonally to its length, forming a topological cylinder. At locations where the dilating cylinder surface contacts solid phase voxels (or sealing planes—see Section 2.6.1), the dilation is stopped. Eventually a closed loop of contacted solid phase voxels encircling the cylinder will form. This loop is identified as the *perimeter* of the minimal area cross-sectional surface (i.e., the throat) for the path. The MA path voxel having closest average distance to these perimeter voxels is declared the *throat center*. The *throat surface* is constructed from a triangulation using the perimeter voxels and the throat center voxel as vertices. For algorithmic simplicity in determining pore bodies, a 6-connected *throat barrier* of voxels is constructed using the voxels cut by the throat surface and (a subset of) their neighboring voxels.

The Dijkstra based algorithm is computationally expensive, especially in the case of intermediate and high porosity media. To address this problem, the wedge-based algorithm [12, 39] was developed. It proceeds by first minimizing area over approximations to cross-sectional surfaces defined by approximated perimeters that are rapidly computable. It then computes a refined perimeter and surface only for the minimal area cross section. The construction of approximate perimeters is aided through a pre-computation of the local grain boundary (LGB) which determines the (unique) set of grain surface voxels that lie closest to any given MA path. For each voxel v on the MA path, a cylindrical coordinate system is constructed based upon the direction tangential to the path at v and a normal direction determined by the LGB voxel to v . This cylindrical coordinate system is divided into a finite number of angular wedges, and a perimeter voxel chosen in each wedge using the closest LGB voxel lying within the angular limits determined by the wedge. This set of wedge determined perimeter voxels forms an approximate perimeter which, together with v , can be triangulated to form a surface.

For any given path, use of only its LGB is often too restrictive; the LGB must be augmented with the LGBs of neighboring paths. Determination of the appropriate set of neighboring paths can, at times, be non-trivial, and can be a reason for failure of the wedge-based algorithm to locate a throat on a complex channel.

2.6. Performance of the individual throat finding algorithms

Estimates of the accuracy of throat finding algorithms and the relation of accuracy to voxel resolution are usually based upon analysis of simulated sphere packs [3,8,38,39]. In this work we were particularly interested in assessing the robustness of the Dijkstra and wedge based throat algorithms in finding throats in real, intermediate porosity media. It has been shown [38,39] that both algorithms find approximately 98% of the (analytically predicted) throats in a hexagonal close packing of spheres, with the 2% error rate attributable to digitization artifacts. Hexagonal packs are, however, very uniform porous media; all known pore partitioning approaches perform well on regular sphere packs. While random sphere packs have been deemed to be representative of Fontainebleau sandstone [42], they are doubtful models even for other sandstones subjected to a richer array of geological and chemical processes, let alone other rock types and unconsolidated media.

Depending on pore geometry, media of $\sim 50\%$ porosity can be the most challenging for throat construction. Near 50% porosity, the opportunity for increased uniformity in void space cross section increases and the ad hoc (intuitive) approach to determining meaningful local minimum can be problematic. Analysis of polyethylene cores, with their combination of smooth, regular solid surface geometry and intermediate porosity (Table 1), is a challenging test for throat finding. Partitioning of the void space employing only either the Dijkstra-based or wedge algorithms, as originally designed, resulted in pore-network partitions of samples P_0 and P_M for which the largest pore accounted for more than 80% of the entire void space! The reasons for this were traced to: (i) a throat finding success rate (throats found/paths searched) that is too low when applied to intermediate porosity samples; (ii) the inability to find throats near the image boundaries; and (iii) use of a MA-based pore partitioning algorithm that rejected too many throats in order to avoid ambiguities.

Issue (i) was addressed by developing an aggressive approach to finding throats on individual paths. Due to its speed, the wedge-based algorithm was run first. Then, for any path on which the wedge-based algorithm failed, the slower Dijkstra-based algorithm was applied. Any path on which the Dijkstra-based algorithm failed was then analyzed a third time as described in Section 2.6.1 by subdividing it to correct for failures due to curvature and/or torsion induced effects. The resolution of (ii) is discussed in Section 2.6.2. Issue (iii) was addressed by redesign of the post-throat finding, pore-network partitioning algorithm (Section 2.7).

2.6.1. Refining the throat search

The Dijkstra-based throat algorithm dilates a MA path in order to find throat perimeter grain voxels. A sealing plane is imposed at each end of the path to limit axial expansion of the dilating cylinder and to ensure contact only with surface voxels that would comprise an effective local grain boundary. The sealing planes are parallel, with normal vector determined by the vector joining the path end points. Sealing planes are illustrated in Fig. 2a. Note that choosing each sealing plane to be

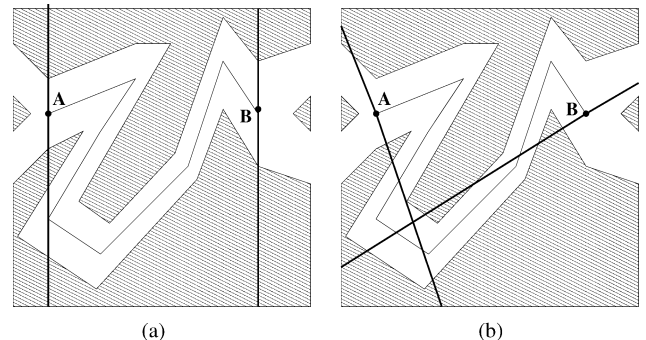


Fig. 2. A 2D sketch of a pore channel corresponding to a MA path AB with sealing planes used to delimit the throat search. In 2D, sealing planes are straight lines, here indicated by the two solid dark lines passing, respectively, through the MA end points A and B. The MA path is the lighter solid line following the channel centerline between end points A and B. The purpose of the sealing planes is to act, in concert with the grain surface, to constrain the propagation of a grassfire algorithm, begun on the MA path, to stay within the pore channel in question. (a) Effective sealing is established when the sealing planes are set orthogonal to the end-point to end-point vector \vec{AB} (vector not shown). (b) Incorrect sealing can result if each sealing plane is separately set orthogonal to the local MA direction at each path endpoint.

locally orthogonal to the path at each end can result in undesirable crossing of the sealing planes as illustrated in Fig. 2b.

The sealing plane direction determination inherently assumes that the end-point to end-point vector is generally representative of the path local orientation. As MA paths associated with porous media curve in space, there will be cases where the sealing planes at path ends will not only cut through the channel containing the MA path, but also the MA path itself. Hence a detected throat may not minimize over all the possible cross sections and, in complicated channel geometries, throat finding may fail. In the polyethylene cores, this effect is very strong.

We subdivide difficult MA paths to correct for this effect. A path is divided into smaller segments, and the Dijkstra-based throat algorithm run on each segment. Over all the segments of a path, that cross-sectional surface having minimal area is accepted as the throat for the path. Points of local maxima in path curvature and torsion (Section 2.4.1) are natural candidates for segment delimiters. In our experience, based upon number of throats successfully determined, delimiting points determined by local maxima in curvature works better than either local maxima in torsion or by simply dividing paths into sections of equal predetermined length.

2.6.2. Boundary effects

The boundaries of the image domain truncate pore channels. As a result, especially if the channel is (roughly) parallel to the boundary, there is usually inadequate information within the image region to correctly locate a throat; frequently no throat is found. The consequence of missing throats on such boundary channels is the appearance of very large pores lying along the image boundary, as shown in Fig. 3. Unlike sandstones (porosities seldom exceeding 25%), in high porosity cores boundaries have a profound effect on pore partitioning. As an example, in a 256^3 volume of 49% porosity polyethylene, missing throats in boundary truncated channels produced a pore which extended

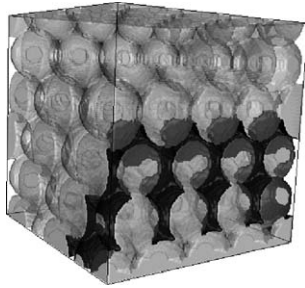


Fig. 3. A large boundary pore (whose surface is delineated in dark gray) located in a hexagonal close packing of spheres (delineated by transparent surfaces) occurring as a result of the inability to determine throats in channels truncated by the image domain. This single pore touches 4 boundaries of the image domain. The volume displays a digitized 128^3 voxel packing of spheres of 32 voxel diameter.

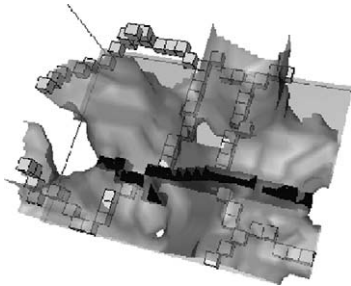


Fig. 4. View of a throat from the P_O core that intersects two different MA paths. Throat barrier voxels are dark, MA voxels are outlined by edges, and the pore–grain interface surface is transparent gray.

along all 6 boundaries of the volume and contained 70% of the pore volume.

We therefore argue that more accurate pore partitioning in finite sized image samples is obtained if the image boundaries are “sealed” with an external layer of “grain” voxels. This allows the throat finding algorithms to work as designed. In the polyethylene example just quoted, with sealed sides the largest pore contained 10% of the pore volume but, more significantly, this large pore lay in the interior of the imaged domain (i.e., it was not in contact with any boundary).

Sealing the boundaries makes some physical sense. Flow experiments commonly performed in rock cores are run under conditions in which the cylindrical sides of the cores are sealed with a sleeve. Our image boundary sealing procedure is analogous. As a technical note, when acquiring statistical information on pores and throats (e.g., size distributions, etc.) the user has the option of ignoring information for pores and throats that contact the sealed surface, in deference to the fact that they are imperfectly computed.

2.6.3. Geometric complexity and throat intersections

A point we stress in this paper is that geometric complexity can lead to intersection behavior by throats. In our analysis of the polyethylene cores (and to a more limited extent in the sandstone samples) we encounter:

- (1) throats that intersect two or more MA paths, as demonstrated in Fig. 4;

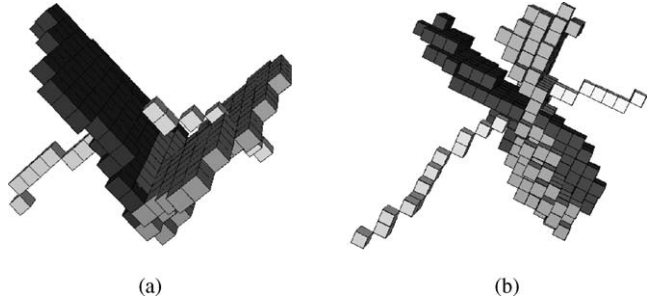


Fig. 5. Examples of (a) V and (b) X configuration throat barrier intersections. In each case the two throats barriers involved are respectively shaded dark and gray. Also shown, in lightest gray tones, are the MA voxels associated with each throat path.

- (2) throats that intersect branch clusters;
- (3) throat barriers that touch or cross.

Throat barriers often touch in a “V” configuration analogous to that depicted in Fig. 5a. V configurations result from throat surfaces that approach sufficiently close to each other so that finite voxel volume effects cause their barriers to touch. “X” configurations (e.g., Fig. 5b), where two throats are detected as crossing regardless of finite voxel size effects, occur less frequently. Complicated 3D geometry can certainly lead to local minimal cross-sectional areas that cross each other. The interpretation of both throats in the X as valid throats in a pore–network decomposition of the void space is not appealing. Resolution of the issues of throat intersections is dealt with in Section 2.7.

2.7. Pore partitioning

Once throats have been identified, the MA provides an alluring search structure on which to identify individual pores and organize the pore–throat network (which pores connect to which through what throats). The occurrence of throats which intersect branch clusters or throats intersecting more than one MA path reduces the effectiveness of the MA for this organization. We therefore employ the following algorithm to organize a topologically correct pore–throat network and reject inconsistent throat topologies (such as intersections):

- (1) In the image domain, void voxels are labeled 0, grain voxels are labeled G (a positive integer), and the barrier voxels for throat i ($i = 1, \dots, N$) are labeled with the negative integer $-i$.
- (2) The pore space is partitioned into M connected regions (called components) separated by throat barrier and grain voxels as follows:
For $j = 1, \dots,$
 - Find a 0 voxel.
 - Run a 26-connected grassfire algorithm from this voxel that iterates only through 0 voxels.
 - Relabel, with the value $G + j$, each voxel “burned” by the grassfire.
 - Repeat until there are no more 0 voxels.

- (3) For each throat barrier, record the components that are incident upon (i.e., are 26-connected to) it.
- (4) Regardless of the number of other throat barriers it may touch, consider as topologically valid any throat having either two incident components (i.e., the throat separates two distinct pore regions) or one incident component (the throat is “interior” to a single component). These throats are retained for now.
- (5) Those throats with more than two components in the neighborhood generally exist because of undesirable intersections with other throats, such as Fig. 5b. We tag such throats and order them by area. This area-ordered list is processed starting with the smallest area throat. A throat in this list is retained if it is not in contact with any other retained throat (tagged or untagged), otherwise it is deleted.
- (6) Steps (1)–(3) are repeated using only the throats retained in steps (4) and (5).
- (7) Any throat having other than two incident components, now does so for reasons other than intersection with other throats. All such throats are now deleted.
- (8) Steps (6) and (7) are repeated (using only throats retained from the previous iteration of (6) and (7)) until no throat is tagged.
- (9) Steps (1) and (2) are repeated using the remaining throats, all of which separate only two different components. These component regions are identified as pore bodies from which pore properties (volume, surface area, coordination number) are measured.

Steps (4) and (5) in the network algorithm remove any throat-throat intersections. Steps (6)–(8) remove other topological inconsistencies in the network. Step (9) finalizes the final pore-throat network. The network algorithm is robust; it provides a topologically consistent pore–throat network by deleting a minimal number of throats that create ambiguities.

2.8. Pore characterization

Our determination of distributions for pore volume, throat area, coordination number and pairwise correlations between these geometrical parameters has been described elsewhere [6,7]. We have recently implemented [26] the ability to compute principal diameters for pores and throats, and surface area and a shape factor for pores. We briefly review these abilities here.

The center-of-mass location and the three principal directions are determined for each pore using a moment-of-inertia analysis. Thus the principal directions always form an orthogonal basis local to each pore. Three principal diameters are determined for each pore by measuring the pore width through the center of mass along each of the principal directions. The diameters are labeled D_1 , D_2 and D_3 in decreasing length. Analogously, two principal diameters are computed for throats using the throat barrier voxels.

The surface area of each pore is the area of the triangulated interface which separates the void space of the pore from the rock/throat voxels sealing that pore. (The interfacial surface

Table 3
Registration results for the image sequences for the two cores

P_O						P_M		
Water (pv)	Shift	f_O	Oil (pv)	Shift	f_O	o:w fluid ratio	Shift	f_O
0.54	(2, 1, 0)	0.66	0.54	(4, 3, 0)	0.17	90:10	(0, -3, 0)	0.73
1.08	(2, 2, 0)	0.29	1.08	(4, 4, 0)	0.67	80:20	(0, -2, -2)	0.73
1.61	(3, 2, 0)	0.24	1.61	(4, 4, -1)	0.68	50:50	(1, 3, -2)	0.62
2.69	(3, 2, -1)	0.18	2.69	(4, 4, -1)	0.69	0:100	(-1, 7, -5)	0.18
5.38	(3, 3, -1)	0.17	5.38	(4, 5, -1)	0.68	100:0 ^a	(-1, 6, -4)	0.83
10.8	(3, 3, -1)	0.15	10.8	(4, 5, -1)	0.69			
64.5	(4, 3, 0)	0.09	64.5	(4, 5, -1)	0.71			

^a Injection following 0:100 flood.

area between fluid phases is also measured from a triangulated surface.) Each triangulated surface is obtained using the marching cubes algorithm [43,44]. The application and accuracy of marching cubes to the computation of interfacial area in porous medium systems was considered by Dalla et al. [45]. Based upon volume and surface area measures, we have proposed [26] a fully 3D shape factor, $G_{3D} \equiv V/S^{1.5}$, where V and S are respectively pore volume and surface area.

3. Results and discussion

3.1. Image registration

In order to segment the fluids in the pore space, it is necessary to begin with solid/void space segmentation. As the solid/void segmentation is performed on the oil saturated image (with the remainder of the images in the flooding sequences inheriting the solid/void segmentation from the oil saturated image), registration of the images in the sequence is the first analysis step. Images in the P_M core sequence were registered using four 200^3 voxel subregions. In the smaller P_O image, finding four disjoint 200^3 voxel subregions containing only polyethylene, water and oil phases is not possible. Therefore two disjoint, 200^3 voxel subregions and one 300^3 voxel subregion that overlapped somewhat with the two smaller subregions were employed. The registration results are presented in Table 3. One measure of the quality of the registration is to compare the maximized value of the oil fraction (columns labeled f_O in Table 3) determined from the (200^3 and 300^3 voxel) registration subregions with the final oil fractions (computable from Table 4) obtained from the fluid segmentation for each entire image. Agreements are within a few percent.

3.2. Image segmentation

Following image registration, the oil saturated image for each core is segmented to identify grain/void voxels. The inset plot in Fig. 6 shows the attenuation coefficient histogram for the oil saturated image of the P_M sample. The lower peak corresponds to the polyethylene core, the upper peak corresponds to oil phase. The T_0 and T_1 values used in the grain/void segmentation are indicated. (These are the same values used to register

the image sequence.) From the segmentation, the porosity of the imaged region of the P_M core was determined to be 50.2%. While this is 10% different from the bulk porosity (Table 1) measured from larger cores (6 inch length, 1.5 inch diameter), experience leads us to believe that the subvolume porosity is accurate to within a few percent, and that 10% porosity variations within subregions of the polyethylene samples are not unexpected.

The main plots in Fig. 6 show the attenuation coefficient histogram in the void space for the subsequent images in the P_M sequence. Water (lower attenuation value) and oil (higher attenuation value) peaks are clearly visible. Measured water saturations obtained from the segmentation are shown in Table 4 (column 2).

Table 4

Fluid occupation synopsis for the P_M and P_O cores. S_w : water saturation; C_w : fraction of the total water volume occupied by the largest connected water blob. S_a and C_a are analogous measures for the air phase. Values with superscript R refer to measures computed in a reduced void region. See text for detail

Image	S_w	C_w	S_a	C_a	S_w^R	C_w^R	S_a^R	C_a^R
P_M (o:w ratio)								
90:10	0.255	0.679			0.232	0.599		
80:20	0.277	0.849			0.256	0.600		
50:50	0.441	0.958			0.414	0.918		
0:100	0.866	0.998			0.884	0.998		
100:0 ^b	0.176	0.614			0.112	0.036		
P_O water injection sequence								
0.54	0.364	0.939			0.368	0.974		
1.08	0.676	0.986			0.712	0.975		
1.61	0.726	0.994			0.762	0.992		
2.69	0.793	0.996			0.823	0.994		
5.38	0.796	0.996			0.825	0.995		
10.8	0.827	0.997			0.854	0.994		
64.5	0.894	0.999			0.916	0.998		
P_O oil injection sequence								
0.54	0.816	0.997			0.839	0.996		
1.08	0.292	0.945	0.076	0.831	0.251	0.719	0.071	0.782
1.61	0.280	0.935	0.098	0.889	0.233	0.309	0.106	0.929
2.69	0.281	0.938	0.090	0.873	0.230	0.193	0.095	0.858
5.38	0.275	0.948	0.086	0.813	0.218	0.060	0.087	0.560
10.8	0.274	0.932	0.094	0.771	0.229	0.152	0.094	0.788
64.5	0.262	0.933	0.038	0.345	0.214	0.171	0.025	0.020

^b Injection following 0:100 flood.

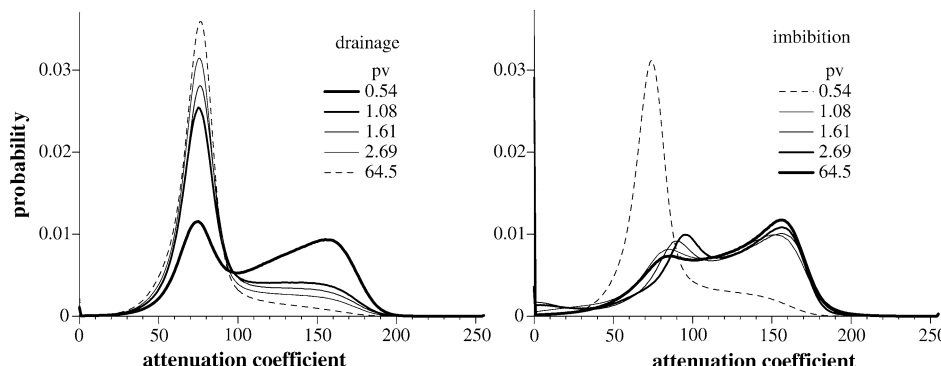


Fig. 7. Pore space histograms for water and oil floods in the P_O core. An air peak around an attenuation coefficient value of zero is visible after 1.08 pv of oil have been injected.

For sample P_0 , grain/void segmentation resulted in a porosity of 43.7%. Attenuation coefficient histograms in the void space of the images of the fluid injection are shown in Fig. 7. (For clarity of presentation, the histograms of two of the images, 5.38 and 10.8 pv injected, from each of the sequences have not been plotted.) In addition to the water and oil peaks, in the right figure (oil injection), a third peak at very low attenuation coefficient values is visible in the histograms. This results from the accidental introduction of an air phase during the oil injection sequence. We attribute this introduction as follows. The preparation room, where fluids were stored and sample set-ups were assembled, was relatively cold, and ambient air most likely dissolved in the hexadecane. When the core and fluids were moved into the experimental area, the hutch was warmer and the gas came out of solution. We attribute the absence of this same effect in the case of the water injection (drainage) sequence to the lower solubility of air in water compared to air in hexadecane. By performing two segmentation steps, we have been able to segment all three fluid phases in the void space of each image. (The first step segments void space voxels into oil/other fluid. The second step segments the “other fluid” voxels into water/air.) An example of this triple-fluid segmentation is shown in Fig. 8. Water and air saturations determined from the segmentations are given in Table 4, columns 2 and 4.

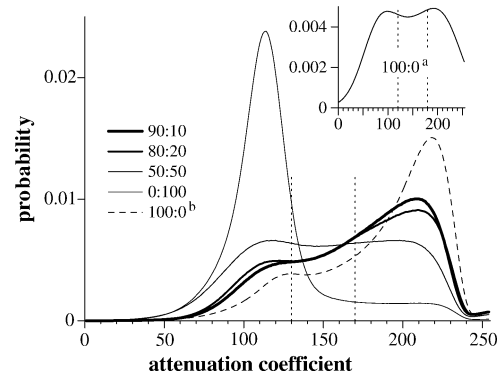


Fig. 6. Attenuation coefficient histogram for the void space in the P_M core imaged at fixed fractional flow conditions. Vertical dotted lines indicate the T_0 and T_1 threshold values used in the segmentation algorithm to segment water and oil phases. (Inset) Attenuation coefficient histogram for the image of the oil saturated P_M core. Vertical dotted lines indicate the T_0 and T_1 threshold values used in the segmentation algorithm to segment pore and grain space.

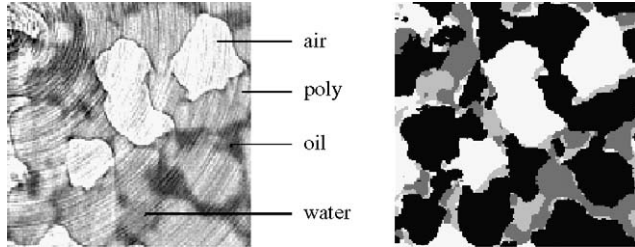


Fig. 8. Fluid distribution in a $150 \times 150 \times 1$ subregion after 1.61 pV oil injection during the drainage sequence in P_O . (Left) the tomographic data; (right) the segmented image.

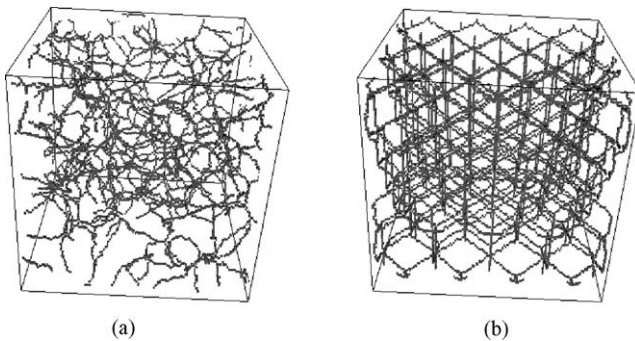


Fig. 9. Comparison of MA's from a 128^3 voxel subvolume of (a) P_O and (b) an HCP of spheres. Sphere diameters are 32 voxels which, assuming the same voxel size as for the P_O data, would imply spheres of $131 \mu\text{m}$ diameter.

Artifacts in fluid segmentation are harder to evaluate than in pore–grain segmentation. Isolated clusters of grain phase voxels in the pore space are unphysical; we handle these by converting them to void phase. Likewise, isolated pore space cavities are inaccessible to fluid flow; for all practical purposes they can be converted to grain phase, which we do. (Such conversions change the overall porosity by less than a minor fraction of a percent.) In segmenting fluids, these arguments do not apply. Consider, for example, disconnected fluid phase blobs of size 5 voxels or less. While there are significant numbers of such blobs of either phase type, they occupy an extremely negligible total fraction of pore space. We therefore choose to retain all fluid phase blobs. However, we avoid computing number density distributions when characterizing fluid blobs in order to protect our results against fluid segmentation errors.

Table 5

Statistics on throat processing. All entries are expressed as a percentage of the total number of MA paths

Sample	Throat detection method			Total	Deleted	Retained
	Wedge	Dijkstra	Subdivision criterion			
	Curvature	Torsion				
P_O	68.4	12.6	7.0	—	88.0	18.2
P_M	66.15	11.55	7.8	0.6	86.1	25.8
						60.3

3.3. Medial axis

The MA provides a searchable network utilized by the throat finding algorithms. Fig. 9 contrasts the MA of the void space obtained from a subregion of sample P_O with that obtained from a hexagonal close packing (HCP) of spheres of uniform radius.

After close cluster merging and dead-end path trimming, tortuosity distributions for the remaining MA paths in P_O are presented in Fig. 10. For comparison purposes, results obtained from the HCP of spheres of Fig. 9 are also displayed. The preponderance of higher tortuosity paths in the rock sample supports the need for employing the path subdivision algorithm (Section 2.4.1) to robustly determine throats in difficult channel geometries. Curvature and torsion (average values for each path) distributions for MA paths in P_O are therefore presented in Fig. 10 where they are compared with results obtained from the HCP of spheres.

3.4. Throat processing

Table 5 summarizes details on throat identification in the two samples. In sample P_O , throats were found for 88.0% of the MA paths. The first pass (wedge) algorithm found throats on 68.4% of the MA paths; the second pass (Dijkstra) algorithm found throats on 40% of the paths for which the wedge algorithm failed (i.e., on 12.6% of all paths). The third pass, employing the Dijkstra algorithm with path subdivision based on the maximum curvature criterion, found throats on 37% of the remaining paths (representing 7% of all paths). 18.2% of all paths had a throat which was rejected by the network resolving algorithm; roughly half of these rejections were due to intersecting throats, the remainder due to other topological inconsistencies. Throats were retained on 69.8% of all paths in

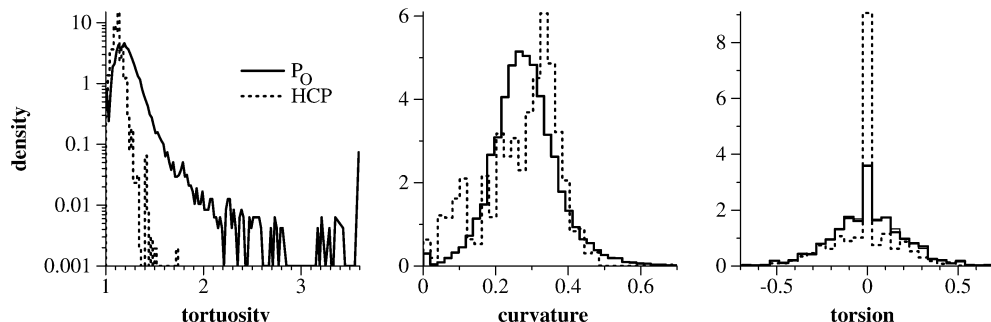


Fig. 10. MA path tortuosity, curvature and torsion (the latter two are path averages) for sample P_O compared with distributions from an HCP of spheres. Results for sample P_M are very similar to P_O .

the P_O sample and on 60.3% in the P_M sample. In both samples, roughly 80% of the retained throats were located using the first pass (wedge) algorithm.

As an illustration of void complexity in these cores, Fig. 11 depicts one of the largest interior pores (0.004 pv) in the final network of sample P_O that was not further subdivided by the throat algorithms utilized here. This pore has 37 neighbors which it contacts through 56 throats (the greatest contact frequency is five times with a single neighbor). The MA of the pore interior is shown separately to illustrate the complexity of the pore.

3.5. Void space characterization

Table 6 summarizes some detail on the pores determined by the network model. In P_O , 50.6% of the void space consisted of pores that lie in the interior of the imaged region (did not

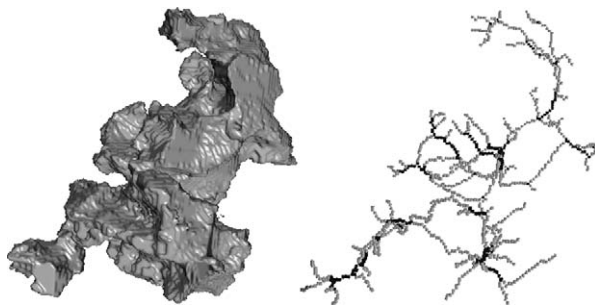


Fig. 11. (Left) the surface of a large pore ($0.012 \text{ mm}^3 = 0.004 \text{ pv}$) in the P_O core. (Right) the MA of the pore interior. MA path voxels are gray, branch cluster voxels are black.

touch the boundary). In contrast interior pores only accounted for 35.9% of the pore space in the larger porosity P_M image. In both samples, the single largest pore (by volume) touched the boundary. The largest interior pores found were more than 50% smaller. This again points to the difficulty in determining throats on channels that are truncated by the image boundary.

Distributions of pore volume, surface area, throat area for interior pores and throats are presented in Fig. 12. For comparison, distributions determined from an 18% porosity Berea sandstone core of similar image size [26] are superimposed. While the pore volume and surface area distributions for polyethylene are more symmetric than the Berea, consistent with the more homogeneous nature of the polyethylene, these two distributions are qualitatively similar to those for Berea. This similarity of pore structure is one reason the polyethylene cores were chosen for study. The polyethylene/Berea throat area distributions are less similar, reflecting the larger porosity (wider channels) of the polyethylene cores.

Distributions for pore principal diameters and effective pore radius (radius of sphere of equivalent volume) of interior pores in P_O are shown in Fig. 13. While less pronounced than noticed in the Berea study [26], there is still qualitative similarity between the distribution of effective pore radius and that of

Table 6
Pore network summary

Sample	Total pores	Interior pore volume	Largest pore volume	
			Boundary	Interior
P_O	4629	50.6%	2.2%	1.0%
P_M	9195	35.9%	4.5%	0.6%

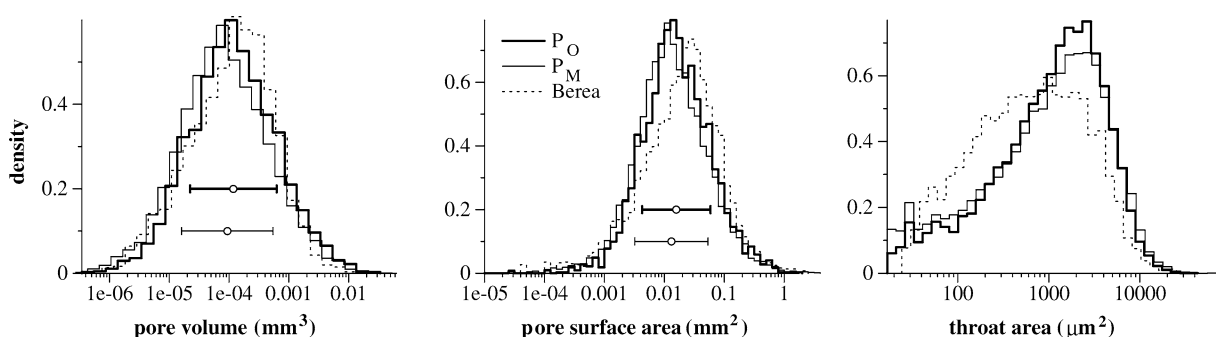


Fig. 12. Distributions of volume and surface area for interior pores, and of throat area, for the P_O core.

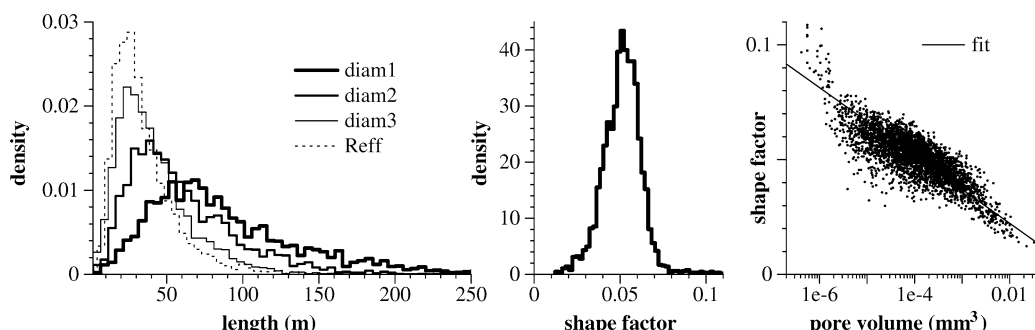


Fig. 13. Distribution of pore diameters and effective radius (left) and shape factor (middle) for internal pores in the P_O core. (Right) correlation between pore shape factor and volume.

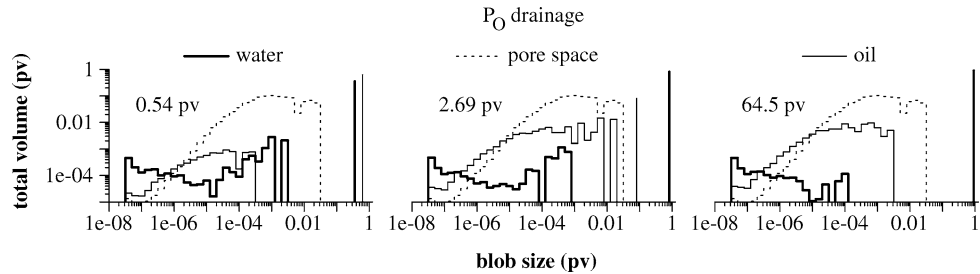


Fig. 14. Distribution of water and oil blob sizes for selected images from the drainage sequence in the P_O core.

smallest pore diameter. The middle figure displays the distribution of the 3D shape factor G_{3D} . Finally the right figure shows the existence of a strong linear correlation between G_{3D} and $\log V$. The trend of the correlation is not unexpected, as the volume:surface ratio is certainly expected to decrease as pore volume increases. For brevity we do not show principal diameter and shape factors (defined as A/P^2 where A is area and P is perimeter [46]) calculated for throats.

3.6. Fluid connectivity and pore scale saturation

Of fundamental interest is the partitioning of the wetting (oil) and non-wetting phases in the pore space at the fluid states studied. Due to the doping, there is excellent attenuation coefficient differentiation between the oil and the other phases. As air has extremely low values of attenuation coefficient there is excellent differentiation between air and the other phases. Differentiation between the polyethylene matrix and water is more problematic; we addressed the identification of polyethylene voxels by image registration and “inheritance” from the first (oil saturated) image in a sequence. Nevertheless, small (even sub-voxel) shift errors in registration can result in surface polyethylene voxels being misidentified as water. *To isolate such errors, fluid partitioning analysis was performed twice, the first time using all void voxels in each image, the second time ignoring any void voxel that abuts a polyethylene voxel.* We refer to the second analysis as occurring in the reduced void region. For the P_O (P_M) sample the reduced void region occupied 66.3% (70.1%) of the total void volume.

As a technical note, since oil is the wetting fluid, oil voxels were treated as 26-connected. Voxels of the water, and where applicable, the air phases are treated as 6-connected during the fluid analysis.

The results of the fluid analysis are summarized in Table 4. The columns labeled S_w and S_w^R compare, respectively, the water saturation determined in the entire void space and in the reduced volume. The change is uniformly less than 5%, with the largest changes occurring when the water saturation is small. By this measure, the reduced void region appears typical of the entire void space. In the oil injection sequence in P_O , air saturation values are also compared for the entire and reduced void regions. Again the differences are small.

We now consider the connectivity of each fluid phase. In each image we identify the largest connected blob of each fluid phase. Let C_w denote the fraction of the water volume occupied by the largest connected water blob as analyzed using the en-

tire void space. Let C_w^R denote the fraction of the water volume occupied by the largest connected water blob as analyzed using the reduced void region. If the largest water blob maintains connectivity via thin films clinging to the polyethylene grains, then C_w^R will be much smaller than C_w .

During the drainage sequence in sample P_O there is no significant reduction in the volume fraction of the largest connected blob when analyzed in the reduced void region. However, for the imbibition sequence in P_O there are very significant reductions. The C_w values are uniformly too large and constant in spite of the fact that the core is being driven to residual water conditions. As perfect registration is impossible, we believe that the apparent water film connectivity is due to a small percentage of polyethylene surface voxels incorrectly identified as water. In contrast, the C_w^R values are in accord with the expectation that the non-wetting phase is reduced to occupying disconnected blobs lying in the “center” of the pore spaces as residual non-wetting conditions are approached. For the steady state, fixed fractional flow injections in the P_M core, the differences between C_w and C_w^R are again consistent with expectations of non-wetting phase occupancy. Based upon these results, we feel that our analysis in the reduced void interior is producing accurate measurement of fluid occupation both in terms of fluid volume and fluid connectivity.

We turn our attention to an analysis of the distribution of the fluids in the reduced void regions. Application of a grassfire algorithm can be used to locate each separate (disconnected) blob of each fluid phase. A representative sample of the distribution of blob volumes is graphically summarized in Fig. 14. To clarify the content of the plots, let $B(\alpha, V, \Delta V)$ denote the set of all blobs of phase α having volume between V and $V + \Delta V$. Let $PV_B(\alpha, V, \Delta V)$ denote the total volume of the blobs in B , where PV_B is normalized by the total pore volume (i.e., expressed as a pv). Fig. 14 plots PV_B vs V (with ΔV changing logarithmically with V).

Consider a plot for a single fluid phase. If that phase is dominant in the pore space, the plot shows that a single large connected blob of that phase fills the majority of the void space. As this blob is an isolated event, it is represented by a vertical line ($\Delta V = \delta V$ for this bin). This large blob is accompanied by a rather continuous volume spectrum of smaller blobs of the same phase. (Note that the logarithmic scales of both axes in these plots visually overemphasize the volumetric contribution of the continuous spectrum.) If the phase under consideration is the residual phase, its distribution shows a continuum of small volume blobs with no dominant blob. If a phase is not dominant,

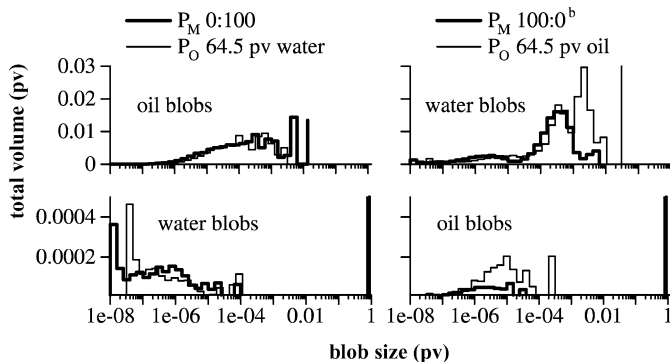


Fig. 15. Comparisons of the distribution of water and oil blob sizes at residual oil (left plots) and residual water (right plots) conditions in the P_M and P_O cores.

but still occupies a significant total fraction of the void space, its distribution typically records a larger connected blob accompanied by a continuous volume spectrum of smaller blobs.

For the wetting phase it can be argued that this continuous distribution of oil blobs is really one or more continuous films of oil clinging to the polyethylene surface. With a voxel size of $4.10 \mu\text{m}$, we are unable to see continuous films, and would only resolve the thicker regions of the films as disconnected blobs.

For comparison, included in each figure is a plot of the pore size distribution. The comparison implies that the largest pore size provides an upper cut-off for the continuum blob distribution, consistent with findings for residual fluid occupation in Berea cores [26].

Images at conditions of residual water and oil saturations were taken on both cores; however the pathway to residual conditions were different in the two cores. Fig. 15 compares the water and oil blob size distributions at residual oil (left plots) and residual water (right plots) conditions in the two cores. At residual oil conditions, both oil and water blob size distributions are remarkably similar between the two cores. (The fact that the volume analyzed in the P_M core is roughly three times larger than in the P_O core explains observed differences in the minimum values of water blob sizes seen in the two cores.) As the total volume occupied by the continuum spectrum is rather small, the similarity of detail in this spectrum between different samples seems to attest to a level of reproducibility of the results. At residual water conditions, the similarity in blob size distributions between the two cores is reduced. This may be due to the appearance of the air phase during oil injection in the P_O core.

The top left plot in Fig. 15 shows the blob size distribution for the wetting phase at wetting phase residual conditions while the top right plot shows the blob size distribution for the non-wetting phase at non-wetting phase residual conditions. The difference between these two is consistent with the expectation of a larger fraction of larger non-wetting blobs at residual non-wetting phase conditions.

We examine the “stability” of the region occupied by the residual phase. Let R_o denote the void space region of sample P_O occupied by the oil phase at residual oil conditions. Similarly, let R_w denote the void space region occupied by the water phase at residual water conditions. R_o occupies 8.4% of

Table 7
Fluid saturations $S_\alpha(R_\beta)$ ($\alpha = o, w, a$; $\beta = o, w$) in two regions R_o and R_w of the P_O core void space

pv	P_O		Imbibition				P_M			
	Drainage		R_o		R_w		Fixed fractional flow		R_o	R_w
	R_o	R_w	S_o	S_w	S_o	S_a	S_w	S_o	S_w	
0.54	97.5	42.9	95.9		94.7		90:10	98.4	42.6	
1.08	96.7	81.0	94.4	1.2	36.4	13.2	80:20	98.2	44.0	
1.61	98.1	86.0	93.9	1.5	36.4	16.8	50:50	93.1	57.5	
2.69	95.6	89.7	93.7	1.1	38.4	15.3	0:100	100.0	97.2	
5.38	95.4	90.2	90.8	1.2	38.8	13.1				
10.8	93.0	92.8	92.0	0.9	43.6	15.5				
64.5	100.0	96.6	90.7	0.6	100.0	0.0				

the pore space, R_w occupies 21.4%. (Regions R_o and R_w have slight overlap; the intersection region is 8.7% of R_o and 3.4% of R_w .) We examine the phase occupancy of these two regions throughout the entire drainage/imbibition flood sequence in P_O . Let $S_\alpha(R_\beta)$, ($\alpha = o, w, a$; $\beta = o, w$) denote the fraction of region R_β occupied by fluid phase α during each stage of the flood sequence. Table 7 tabulates values of $S_\alpha(R_\beta)$. The wetting phase residual region, R_o retains oil saturation levels above 90% throughout the entire drainage/imbibition cycle.

Not unexpectedly, the non-wetting phase residual region R_w demonstrates greater change in phase saturation value throughout the drainage/imbibition cycle. The results indicate that the range between 0.5 and 1.0 pv injected fluid is a critical regime for the R_w region in both cycles. During drainage, by 1.08 pv of injected water, region R_w acquires a water saturation of 81%, however at 0.54 pv, the water occupancy in R_w is only half of this. Similarly during imbibition (oil injection) R_w is able to retain a significant water saturation when 0.54 pv of oil has been injected, but by 1.08 pv injection, the water saturation in R_w drops to 36%. Interestingly R_w retains less than 44% water occupancy during the injection of 10.8 pv of oil; and only when significant (64.5) pore volumes of oil are injected does R_w reach 100% water saturation. This indicates that there is (relatively speaking) significant water (non-wetting phase) movement into this residual fluid region during the later stages of imbibition.

The data for P_M indicates that the process of injection with fixed fluid ratios (involving decreasing oil and increasing water) “mimics” that of a drainage sequence.

As air is introduced accidentally in the imbibition cycle in P_O we largely avoid attempting to analyze the air data. Measured air saturations in regions R_o and R_w are included in Table 7 to make one observation. We assume that air entered the system due to its higher solubility in hexadecane than water, and was consequently released from the oil phase during imbibition. The relatively high air saturation values in R_w appear consistent with this assumption and the observation that there is, during imbibition, significant occupation of the region by the oil phase. However, we find low air saturation values in region R_o , where oil occupancy is uniformly large. We attribute this to preferential wetting between the polyethylene surfaces

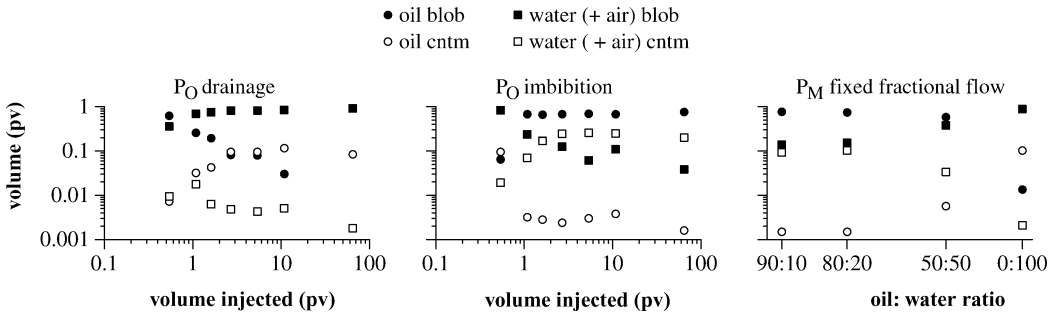


Fig. 16. Total volume of fluid in the dominant blob (solid points) and the continuum spectrum (open points) for each fluid phase during the injection sequences.

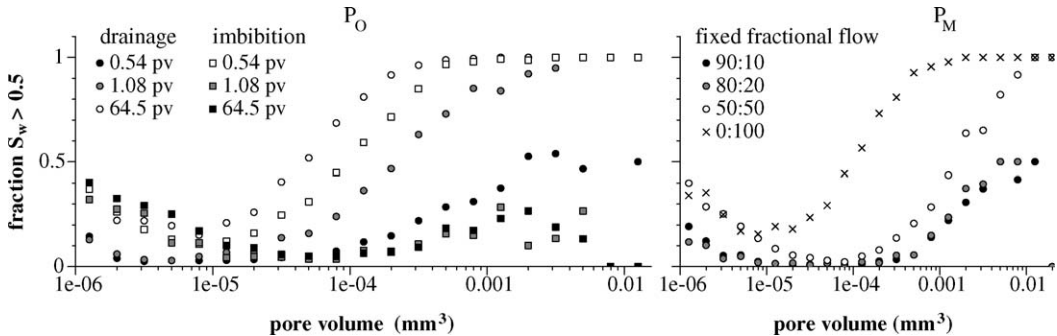


Fig. 17. Fraction of pores with water saturation above 50% vs pore volume for the P_O core. All quantities are calculated for the reduced void region.

and oil; the resulting capillary forces would tend to displace any air from the R_o region.

Fig. 16 traces the total volume of fluid both in the dominant blob and in the continuum blob spectrum for each phase through the separate injection sequences. For the imbibition sequence in P_O , we have pooled the volume results for both non-wetting (water + air) phases. A dominant feature in each plot is the “cross-over” behavior produced as the largest blob of resident fluid decreases in size while the largest blob of displacing fluid grows. In either drainage or imbibition, we observe cross-over to occur before one pv of the displacing fluid is injected. Using fixed fractional flow rates however, the cross-over behavior occurs at 50:50 fluid injection ratio. The cross-over behavior in the total volume of the continuum spectrum mirrors that of the dominant blobs.

The ability to identify single pores enables correlation of changes in fluid distribution with pore size. The fractional fluid occupancy (saturation) can be computed on a pore-by-pore basis and occupancy summarized as a function of pore volume. (Recall that we are analyzing only the reduced void region.) Let $P(V, \Delta V)$ denote the set of pores with (reduced region) pore volume in the range $(V, V + \Delta V)$. Let $F(0.5, V, \Delta V)$ denote the fraction of pores in P having water saturation greater than 0.5. Fig. 17 plots $F(0.5, V, \Delta V)$ vs V (with ΔV varying logarithmically with V). The left figure plots (selected images from) a full drainage–imbibition cycle in P_O . As expected, during drainage, pores fill primarily from the largest size. By 0.54 pv of injected water, 50% of the pores of size greater than 0.002 mm^3 have water saturation exceeding 0.5; by 1.08 pv of injected water, virtually 100% of the pores of size greater than 0.001 mm^3 have water saturation exceeding 0.5. By residual water conditions, 100% of the pores of size greater than 0.0003 mm^3 have

water saturation exceeding 0.5. This effect is reversed under imbibition, by the time 1.08 pv of oil have been injected, only 50% of the pores of size greater than 0.002 mm^3 have water saturation exceeding 0.5.

Under fixed fractional flow injection, the behavior is qualitatively the same, though the rate at which large pores fill with water is decreased, presumably due to the fact that fixed fractional flow allows for competing oil and water flow paths.

Fig. 18 plots the measured interfacial surface area between the oil phase and the non-wetting phase (water or water + air) during the fluid injection sequences. (We plot surface area versus oil saturation (computed in the reduced void volume). Table 4 can be used to correlate each entry with the amount of fluid injected.)

We plot our P_O results separately for the drainage and imbibition cycles, the fixed fractional flow P_M data are shown on both plots. Our data are compared with published experimental results based upon interface sorbing anionic surfactants [47–50]. We have found no experimental data on oil–water interfaces for floods in oil-wet polyethylene cores; we therefore compare with available oil–water and air–water measurement in water wet sand- and glass-bead packs.

The drainage experiment results of Kim et al. [47] and Schaefer et al. [49,50], as well as network flow model results (e.g., [51]), suggest essentially linear increase in the wetting–nonwetting interfacial area with decreasing wetting phase saturation until a low wetting phase saturation is reached, after which the interfacial area must fall to zero. (We have plotted the data of Kim et al. in its entirety; the data of Schaefer et al. is represented only by least-squares linear fits reported for their data.) The network model results suggest the critical wetting saturation is in the range 0.2–0.3 [51], the experimental results

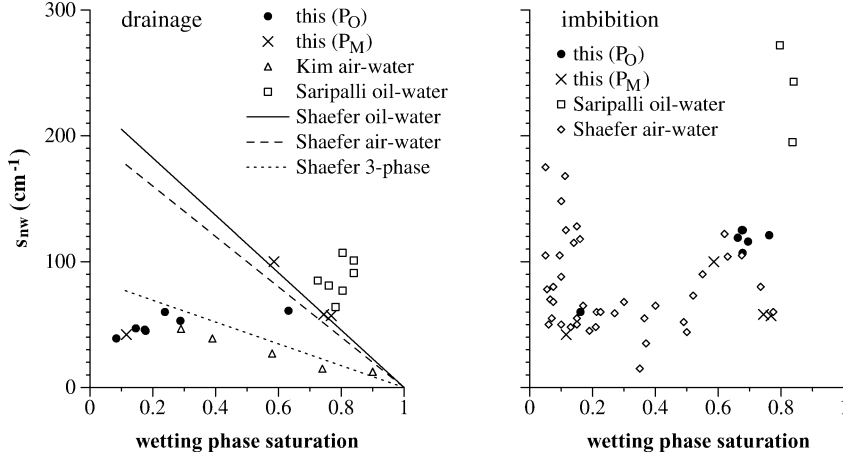


Fig. 18. Interfacial area σ_{nw} between the oil (wetting) and the non-wetting phase (water, water + air) in the reduced void region.

observe linear increase down to wetting saturations of 0.3 [47] and 0.1 [49,50]. Our drainage data, which is sparse in the linear range (high wetting phase saturation), as well as our fixed fractional flow data (which is sparse in the low wetting phase saturation), suggest decreasing interfacial areas below wetting saturation of 0.3.

Unlike drainage, the imbibition experimental results are not simply characterizable. Due to the appearance of an air phase, our imbibition results are three-phase. We therefore measure the total oil surface in contact with water or air. The results are very consistent with the results of five experimental air–water interface data sets (shown in their entirety) of Shaefer et al. [49].

It is fairly obvious that the segmentation algorithm as well as finite voxel size are critical in determining surface area accuracy. Segmentation at finite voxel size smooths interfaces and sufficiently thin films are not observed. Both of these would result in systematically low estimates for fluid–fluid interfacial area.

4. Summary

In the extraction of pore network descriptions from 3D images of porous media, we have argued for the need, especially in intermediate ($\sim 50\%$) porosity materials where 3D geometric complexity can contradict naive expectations, to ensure that throats (located either explicitly or implicitly) do not intersect in a manner that causes a single throat to separate other than exactly two pores. Explicitly incorporating such checks, we have demonstrated a pore-network extracting package of algorithms that is applicable to media (such as unconsolidated soils) of such porosities.

Using these algorithms, we have performed an analysis both of the pore-network of polyethylene core images as well as the partitioning of wetting and non-wetting phases imaged in the pore space. In particular we have demonstrated the ability to resolve three fluid phases (a gas and two liquids) in the pore space as well as the solid phase of the medium.

We have demonstrated the capability of extracting quantitative information (blob sizes, individual pore occupancies, occupancies in significant subregions of the core, interfacial

contact areas) on the fluid partitioning at residual fluid conditions and at fixed fluid states on a state–space path to residual conditions. In general our results confirm that, at the pore level, during drainage or imbibition, the injection of one PV of invading fluid produces the most significant partitioning changes. By comparing drainage and imbibition with fixed fractional flow injections, our results suggest that fluid partitioning at residual conditions may have features that are relatively independent of the phase space path under which residual conditions are approached.

Our interfacial contact area results are in qualitative agreement with magnitudes and trends shown in experimental and modeling data, though our data is sparse in covering the range of phase saturations.

Acknowledgments

This work was supported by the US Department of Energy Geosciences Program, Grants DE-FG02-92ER-14261 (MP, WBL) and DE-FG02-05ER-15635 (WBL); by NPTO and NETL of the US Department of Energy, the State of New Mexico, ConocoPhillips, Marathon, and ExxonMobil (RSS).

References

- [1] J.-F. Thovert, J. Salles, P.M. Adler, J. Microscopy 170 (1993) 65.
- [2] P. Spanne, J.-F. Thovert, C.J. Jacquin, W.B. Lindquist, K.W. Jones, P.M. Adler, Phys. Rev. Lett. 73 (1994) 2001.
- [3] H.Q. Zhao, I.F. MacDonald, M. Kwiecien, J. Colloid Interface Sci. 162 (1994) 390.
- [4] W.B. Lindquist, S.-M. Lee, D.A. Coker, K.W. Jones, P. Spanne, J. Geophys. Res. B 101 (1996) 8297.
- [5] C.A. Baldwin, A.J. Sederman, M.D. Mantle, P. Alexander, L.F. Gladden, J. Colloid Interface Sci. 181 (1996) 79.
- [6] W.B. Lindquist, A.B. Venkatarangan, Phys. Chem. Earth A 25 (1999) 593.
- [7] W.B. Lindquist, A.B. Venkatarangan, J.H. Dunsmuir, T.-F. Wong, J. Geophys. Res. 103 (2000) 21508.
- [8] Z. Liang, M.A. Ioannidis, I. Chatzis, J. Colloid Interface Sci. 221 (2000) 13.
- [9] R.I. Al-Raoush, K. Thompson, C.S. Willson, Soil Sci. Soc. Am. J. 67 (2003) 1687.
- [10] D.B. Silin, G.D. Jin, T.W. Patzek, J. Petrol. Technol. 56 (2004) 69.

- [11] M.A. Knackstedt, C.H. Arns, A. Limaye, A. Sakellariou, T.J. Senden, A.P. Sheppard, R.M. Sok, W.V. Pinczewski, G.F. Bunn, SPE Paper 87009, Soc. Petrol. Eng., Richardson, TX (2004).
- [12] H. Shin, W.B. Lindquist, D.H. Sahagian, S.-R. Song, Comput. Geosci. 31 (2005) 473.
- [13] R.I. Al-Raoush, C.S. Willson, J. Hydrol. 300 (2005) 44.
- [14] B.P. Flannery, H.W. Deckman, W.G. Roberge, K.L. D'Amico, Science 237 (1987) 1439.
- [15] J.J. Buckles, R.D. Hazlett, S. Chen, K.G. Eggert, D.W. Grunau, W.E. Soll, Los Alamos Sci. 22 (1994) 112.
- [16] B.B. Ferreol, D.H. Rothman, Trans. Porous Media 20 (1995) 3.
- [17] F.M. Auzerais, J.H. Dunsmuir, B.B. Ferreol, N. Martys, J. Olsen, T.S. Ramakrishnan, D.H. Rothman, L.M. Schwartz, Geophys. Res. Lett. 23 (1996) 705.
- [18] M.E. Coles, R.D. Hazlett, E.L. Muegge, K.W. Jones, B. Andrews, B. Dowd, P. Siddons, A. Peskin, P. Spanne, W.E. Soll, SPE Reserv. Eval. Eng. 36531 (1998) 288.
- [19] M. Hilpert, C.T. Miller, Adv. Water Resour. 24 (2001) 243.
- [20] C.H. Arns, M.A. Knackstedt, W.V. Pinczewski, W.B. Lindquist, Geophys. Res. Lett. 28 (2001) 3361.
- [21] J.Y. Arns, C.H. Arns, A.P. Sheppard, R.M. Sok, M.A. Knackstedt, W.V. Pinczewski, J. Pet. Sci. Eng. 39 (2003) 247.
- [22] P.H. Valvatne, M.J. Blunt, Water Resour. Res. 40 (2004) W07406.
- [23] D. Wildenschild, J.W. Hopmans, C.M.P. Vaz, M.L. Rivers, D. Rikard, B.S.B. Christensen, J. Hydrol. 267 (2002) 285.
- [24] R.S. Seright, J.-T. Liang, W.B. Lindquist, J.H. Dunsmuir, SPE Reserv. Eval. Engin. 5 (2002) 355.
- [25] R.S. Seright, J.-T. Liang, W.B. Lindquist, J.H. Dunsmuir, J. Pet. Sci. Eng. 39 (2003) 217.
- [26] M. Prodanović, W.B. Lindquist, R.S. Seright, Adv. Water Resour., in press.
- [27] D. Wildenschild, J.W. Hopmans, M.L. Rivers, A.J.R. Kent, Vadose Zone J. 4 (2005) 112.
- [28] R.I. Al-Raoush, C.S. Willson, J. Contam. Hydrol. 77 (2005) 67.
- [29] M.L. Turner, L. Knufing, C.H. Arns, A. Sakellariou, T.J. Senden, A.P. Sheppard, R.M. Sok, A. Limaye, W.V. Pinczewski, M.A. Knackstedt, Physica A 339 (2004) 166.
- [30] M.J. Kwiecien, I.F. MacDonald, F.A.L. Dullien, J. Microsc. 159 (1990) 343.
- [31] D.P. Lymberopoulos, A.C. Payatakes, J. Colloid Interface Sci. 150 (1992) 61.
- [32] H.Q. Zhao, I.F. MacDonald, J. Microsc. 172 (1993) 157.
- [33] T. Lee, R. Kashyap, C. Chu, Graph. Mod. Image Process. 56 (1994) 462.
- [34] C. Ma, M. Sonka, Computerized Vision Image Understanding 64 (1996) 420.
- [35] W.B. Lindquist, 3DMA General Users Manual, Department of Applied Mathematics and Statistics, Stony Brook University, 1999; [ftp://ams.sunysb.edu/pub/papers/1999/susb99_20.pdf](http://ams.sunysb.edu/pub/papers/1999/susb99_20.pdf).
- [36] W.B. Lindquist, 3DMA-Rock, A Software Package for Automated Analysis of Pore Rock Structure in 3D Computed Microtomography Images; http://www.ams.sunysb.edu/~lindquis/3dma/3dma_rock/3dma_rock.html.
- [37] W. Oh, W. Lindquist, IEEE Trans. Pattern Anal. Mach. Intell. 21 (1999) 590.
- [38] A. Venkatarangan, Geometric and statistical analysis of porous media, Ph.D. thesis, Stony Brook University (2000).
- [39] H. Shin, A throat finding algorithm for medial axis analysis of 3D images of vesiculated basalts, Ph.D. thesis, Stony Brook University (2002).
- [40] J.-F. Delerue, E. Perrier, Z. Yu, B. Velde, J. Phys. Chem. Earth 24 (1999) 639.
- [41] F. Dullien, Porous Media: Fluid Transport and Pore Structure, second ed., Academic Press, New York, 1992.
- [42] M. Gladkikh, S. Bryant, Adv. Water. Resour. 26 (2003) 609.
- [43] J. Bloomenthal, IEEE Comput. Graph. Appl. 5 (1988) 341.
- [44] W. Lorensen, H. Cline, ACM Computer Graphics 21 (1987) 163.
- [45] E. Dalla, M. Hilpert, C.T. Miller, J. Contam. Hydrol. 56 (2002) 25.
- [46] G. Mason, N.R. Morrow, J. Colloid Interface Sci. 141 (1991) 262.
- [47] H. Kim, P.S.C. Rao, M.D. Annable, Water Resour. Res. 33 (1997) 2075.
- [48] K.P. Saripalli, P.S.C. Rao, M.D. Annable, J. Contam. Hydrol. 30 (1998) 375.
- [49] C.E. Schaefer, D.A. DiCarlo, M.J. Blunt, Water Resour. Res. 36 (2000) 885.
- [50] C.E. Schaefer, D.A. DiCarlo, M.J. Blunt, J. Colloid Interface Sci. 221 (2000) 308.
- [51] P.C. Reeves, M.A. Celia, Water Resour. Res. 32 (1996) 2345.